

Density Matrix Renormalization Group Study of Domain Wall Qubits

Guanxiong Qu,¹ Ji Zou,² Daniel Loss,^{1,2,3} and Tomoki Hirotsawa⁴

¹RIKEN, Center for Emergent Matter Science (CEMS), Wako-shi, Saitama 351-0198, Japan

²Department of Physics, University of Basel, Klingelbergstr. 82, 4056 Basel, Switzerland

³RIKEN, Center for Quantum Computing (RQC), Wako-shi, Saitama 351-0198, Japan

⁴College of Science and Engineering, Aoyama Gakuin University, Japan

(Dated: December 17, 2024)

Nanoscale topological spin textures in magnetic systems are emerging as promising candidates for scalable quantum architectures. Despite their potential as qubits, previous studies have been limited to semiclassical approaches, leaving a critical gap: the lack of a fully quantum demonstration. Here, we address this challenge by employing the density-matrix renormalization group (DMRG) method to establish domain wall (DW) qubits in coupled quantum spin-1/2 chains. We calculate the ground-state energies and excitation gaps of the system and find that DWs with opposite chiralities form a well-defined low-energy sector, distinctly isolated from higher excited states in the presence of anisotropies. This renders the chirality states suitable for encoding quantum information, serving as robust qubits. Interestingly, when a magnetic field is applied, we observe tunneling between quantum DW states with opposite chiralities. Through quantum simulations, we construct an effective qubit Hamiltonian that exhibits strongly anisotropic g -factors, offering a way to implement single-qubit gates. Furthermore, we obtain an effective interacting Hamiltonian for two mobile DWs in coupled quantum spin chains from DMRG simulations, enabling the implementation of two-qubit gates. Our work represents a critical step from semiclassical constructions to a fully quantum demonstration of the potential of DW textures for scalable quantum computing, establishing a solid foundation for future quantum architectures based on topological magnetic textures.

Introduction.—Magnetic domain walls (DWs) are quasi-one-dimensional topological defects characterized by a winding number [1]. Their topologically protected spin textures provide robustness, making DWs highly attractive for classical information applications [2]. This potential has spurred significant experimental efforts, leading to recent advancements in the efficient manipulation of DWs with sub-10 nm widths at velocities exceeding 100 m/s [3, 4]. Leveraging mobile DWs as information carriers, racetrack memory offers a promising route to fast and high-density data storage [5].

Beyond classical applications, nanoscale spin textures provide an exciting platform for macroscopic quantum phenomena at low temperatures [6]. With increasing interest in expanding quantum computing platforms, recent proposals have explored the use of nanoscale magnetic textures, such as skyrmions [7, 8] and DWs [9, 10], as qubits. These robust and high-speed topological textures show great potential for functioning as flying qubits [10–13]. Besides, single- and two-qubit gates have been proposed via external fields and current-driven motion [10], laying the foundation for universal quantum computation within existing spintronic technologies. However, while the potential of topological textures as qubits hinges fundamentally on their quantum nature, all previous proposals have been limited to semiclassical treatments, valid for large spin, using collective-coordinate approaches within the continuum limit of the model. This situation is highly unsatisfactory, since spins are intrinsically quantum objects with their quantum properties being crucial to enabling quantum computation in such systems. A fully quantum treatment for

spin-1/2, critical for rigorously establishing the feasibility of topological textures as robust qubits, remains an open and pressing challenge.

In this letter, we address this critical challenge by employing the density-matrix renormalization group (DMRG) method [14–16] to investigate quantum properties of ferromagnetic DW (kink-type) textures in coupled quantum spin chains [17]. By examining the ground-state and low-lying excited-state properties of these DW textures, we find that DW states with opposite chiralities, as depicted in Fig. 1(a), form a well-defined low-energy sector that is well-separated from higher excited states. This isolation enables the encoding of quantum information into the DW chiralities. Remarkably, we observe that the tunneling rate and energy detuning between the two quantum DW chirality states are highly tunable via magnetic fields applied along the y - and x -directions, respectively, characterized by an anisotropic effective g -factor. Furthermore, by restricting to the chirality subspace, we construct an effective Hamiltonian for a single DW qubit, capturing its essential quantum dynamics. Moreover, to demonstrate the two-qubit gate between DWs, we consider two coupled quantum spin chains. By calculating the ground-state and excited-state energies for DWs at varying separations, we construct an effective Hamiltonian for the mobile DWs, enabling the implementation of two-qubit gates. Our work establishes the feasibility of utilizing DW textures for universal quantum computation within a fully quantum framework, surpassing previous studies that relied on semiclassical approaches. This provides a rigorous and solid foundation for leveraging topological textures as promising platforms for future

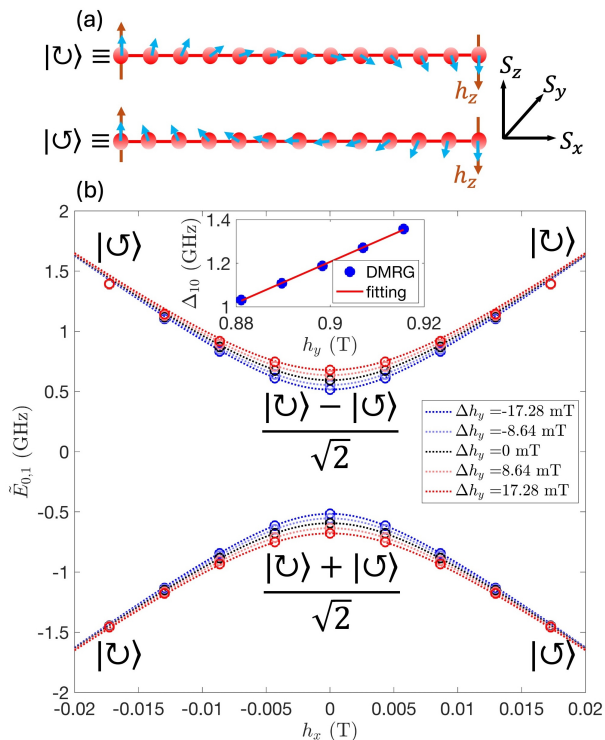


FIG. 1. (a) Schematic illustration of DW chirality states in a single quantum DW. (b) DMRG simulation data (circle) and effective Hamiltonian (dotted line) of DW qubits energy spectra with tuning of external magnetic fields $h_{x,y}$. The inset shows tuning of the qubit splitting Δ_{10} by small variation of h_y . $\tilde{E}_{0,1}$ are energies shifted such that the zero-energy level is aligned with the center of the qubit splitting. Parameters for DMRG simulations are shown in Tab. I.

quantum architectures.

DMRG for quantum DW.—We calculate the ground-state and low-lying excited state energies of a DW texture in an open anisotropic (XYZ) ferromagnetic quantum spin-1/2 chain with N sites, governed by the following Hamiltonian:

$$H_{\text{chain}} = \sum_{i=1}^{N-1} (-J\mathbf{S}_i \cdot \mathbf{S}_{i+1} - K_z S_i^z S_{i+1}^z + K_y S_i^y S_{i+1}^y) + \sum_{i=1}^N (\mu_B h_x S_i^x + \mu_B h_y S_i^y) + \mu_B h_z (S_1^z - S_N^z), \quad (1)$$

where S_i^α denotes the spin-1/2 operators with $\alpha \in \{x, y, z\}$, $J > 0$ represents isotropic ferromagnetic coupling, and $K_{z,y} > 0$ denote easy z -axis and hard y -axis exchange anisotropies, respectively. Here, $h_{x,y}$ is an external magnetic field along the x - or y -axis. To focus on the DW spin texture, the boundary spins ($i = 1, N$) are coupled to pinning z -fields ($h_z \gg J, K_{z,y}$), ensuring a kink-type ground state [17–19]. Such pinning fields can emerge from exchange coupling the boundary spins to magnets with magnetization along $\pm z$ direction. We remark that, in the absence of hard axis anisotropy and ex-

TABLE I. Parameters for DW qubits on coupled spin chains. We use $N = 30$, $J = 25.85$ meV, $K_z = 0.26$ meV, $K_y = 0.1$ meV, $\mu_B h_z = -100$ meV, and $h_y = 0.9$ T for DMRG simulations.

Δ_{10}	g_x	g_y	$J_{\text{in}}^{\text{eff}}$
1.2 GHz	76.2 GHz/T	9.4 GHz/T	278 MHz

ternal magnetic fields ($K_y = 0, h_{x,y} = 0$), Eq. (1) reduces to the XXZ model which can be solved analytically with fixed boundary condition [18] and anti-periodic boundary condition [20, 21] to support DWs. However, introducing a finite K_y renders an analytical solution infeasible.

To characterize the chirality of the DW in a quantum spin chain, we introduce the chirality operators [22–24] on the spin lattice

$$C_\gamma = \epsilon_{\alpha\beta\gamma} \sum_{i=1}^{N-1} S_i^\alpha S_{i+1}^\beta, \quad (2)$$

where $\epsilon_{\alpha\beta\gamma}$ is Levi-Civita symbol with $\alpha, \beta, \gamma \in \{x, y, z\}$. By evaluating the energies of the first few states and their chiralities, we find that, for $K_y > 0$, the ground state exhibits degenerate DW chiralities and importantly is well-separated from higher-energy states. For instance, with $K_y = 0.1$ meV, the gap exceeds 9.6 GHz and remains largely unaffected by the h_y field, even up to 1 T [25]. This large gap between the chirality-state subspace and higher excited states enables the encoding of quantum information within this well-isolated subspace (qubit space). We note that in the XXZ limit the ground state is non-degenerate for N even while doubly degenerate for N odd [17]. However, already a small easy-axis anisotropy K_y sufficiently suppresses these finite-size parity effects [25].

We then investigate the effects of an in-plane magnetic field on the low-energy states using DMRG. The parameters used for the simulations are summarized in Tab. I. We find that applying a strong magnetic field along the y -direction (e.g., $h_y = 0.9$ T) lifts the degeneracy of the chirality states, resulting in a $\Delta_{10} \equiv E_1 - E_0$ in the GHz regime, as shown in the inset of Fig. 1(b). Physically, this magnetic field suppresses the tunneling barrier and facilitates quantum tunneling between the two chirality states [6, 10]. Additionally, in Fig. 1(b), we demonstrate the tunability of the qubit splitting through both a small h_x field and slight variations in the h_y field near the bias field $h_{y,\text{bias}} = 0.9$ T.

We further show the chirality of the DW qubit in a single quantum chain in Fig. 2. When tuning the h_x field, we observe that, interestingly, the DW chiralities perpendicular to the hard-axis anisotropy, C_x and C_z , remain nearly unchanged. In sharp contrast, the DW chirality C_y shifts with the h_x field. At small bias fields, $h_x = \pm 17$ mT, the qubit states (E_0 and E_1) exhibit opposite C_y -

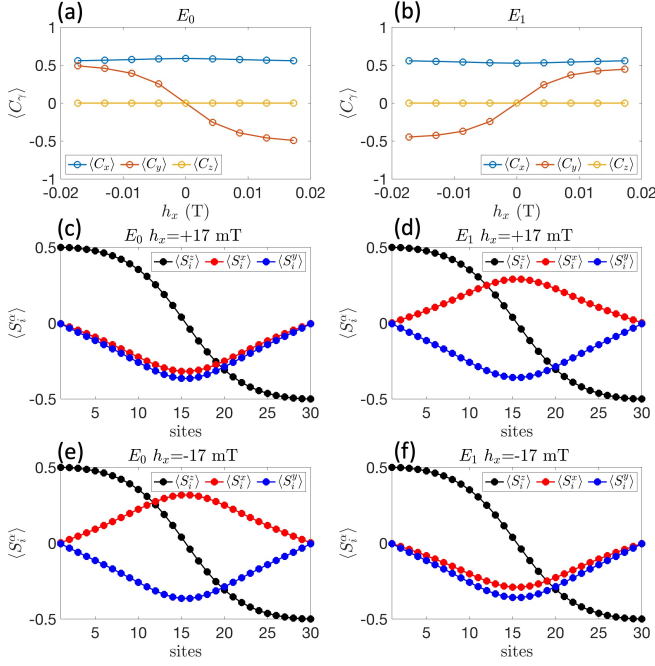


FIG. 2. DW chiralities of a single spin chain with external magnetic fields: (a,b) DW chiralities $\langle C_\gamma \rangle$ tuning by h_x field; (c,d) spin profiles $S_i^{x,y,z}$ with positive bias field $h_x = +17$ mT; (e,f) spin profiles $S_i^{x,y,z}$ with negative bias field $h_x = -17$ mT. DMRG simulation parameters are the same as in Fig. 1.

chiralities, denoted as $|\odot\rangle$ and $|\ominus\rangle$. Flipping the direction of the magnetic field h_x correspondingly reverses the chirality C_y of the qubit states. The spin profiles of a single spin chain, shown in Fig. 2, reveal the C_y -chiralities of DW qubits under small bias fields ($h_x = \pm 17$ mT). Notably, at zero bias field ($h_x = 0$), the qubit states are superposition state of the two C_y -chiralities, resulting in a vanishing expectation value of chirality $\langle C_y \rangle$.

Effective Hamiltonian.—We systematically tune the magnetic field $h_{x,y}$ and find that the qubit splitting Δ_{10} increases exponentially with the h_y field, while it varies linearly with h_x [25]. From the DMRG simulations, we construct an effective Hamiltonian for the DW qubit subspace in a single quantum spin chain:

$$H_1^{\text{eff}} = \Delta_{10}\sigma_z/2 + g_y\Delta h_y\sigma_z - g_x h_x\sigma_x, \quad (3)$$

where $g_{x,y}$ are effective g -factors. Here, $\Delta h_y \equiv h_y - h_{y,\text{bias}}$ denotes a small deviation from the strong bias field, while $\sigma_{x,y,z}$ are pseudo-spin operators defined in the DW chirality subspace spanned by the superposition states $(|\odot\rangle + |\ominus\rangle)/\sqrt{2}$ and $(|\odot\rangle - |\ominus\rangle)/\sqrt{2}$. In Fig. 1(b), we illustrate the agreement between DMRG simulations and the effective Hamiltonian. The linear dependence of the qubit splitting Δ_{10} on h_x is clearly observed, allowing the effective g -factor to be extrapolated as $g_x \approx 76.2$ GHz/T. Similarly, Δ_{10} varies approximately linearly with Δh_y , yielding an effective g -factor of $g_y \approx 9.4$ GHz/T. Thus,

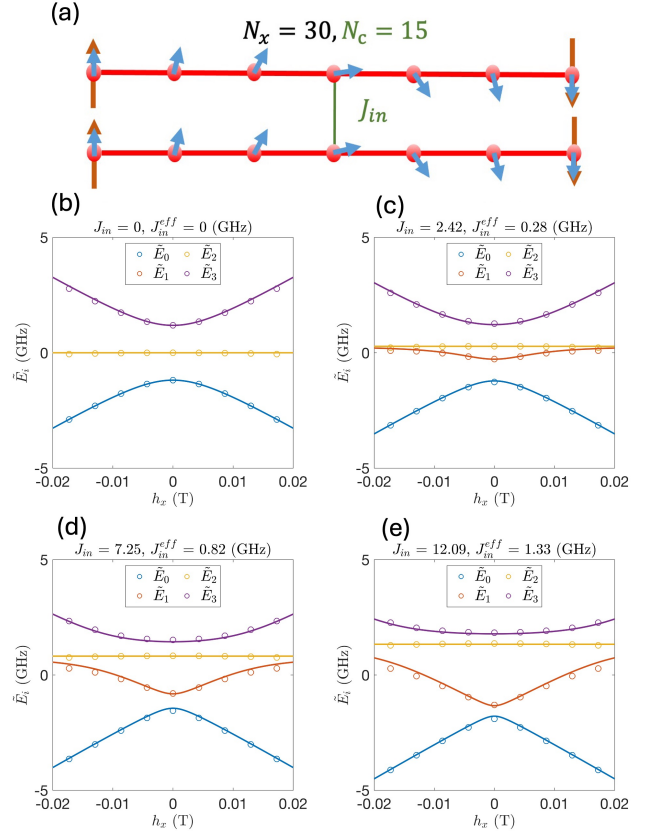


FIG. 3. (a) Schematic illustration of DMRG simulation for two stationary DW qubits. (b-e) Energy spectra of two-qubit subspace for two stationary DW qubits with various single site coupling strength $J_{in} = 0, 2.42, 7.25, 12.09$ GHz, corresponding to 0, 10, 30, 50 μeV . Circles represent DMRG data and line plots represent effective Hamiltonian with $J_{in}^{\text{eff}} = 0, 0.28, 0.82, 1.33$ GHz. Parameters for each DW qubit are the same as in Fig. 1.

a single DW qubit exhibits strongly anisotropic g -factors under magnetic field tuning.

This anisotropic g -factors in Eq. (3) enable the implementation of Rabi-driving and phase-driving mechanisms for a single DW qubit [26]. Here, we demonstrate Rabi-driven rotation on a single DW qubit by applying an oscillating magnetic field $h_x \cos(\omega_x t)$: $H_1^{\text{Rabi}} = \hbar\omega_q\sigma_z/2 - g_x h_x \cos(\omega_x t)\sigma_x$, where $\hbar\omega_q = \Delta_{10}$ is the qubit frequency. In rotating wave approximation, the Hamiltonian reads $\tilde{H}_{1,\text{RWA}} = \hbar\Delta\omega\sigma_z/2 - g_x h_x\sigma_x/2$ with $\Delta\omega = \omega_q - \omega_x$. At the resonance condition $\Delta\omega = 0$, it yields a single qubit rotation around x -axis, $U_{1,z}(t) = \exp[ig_x h_x\sigma_x t/(2\hbar)]$, with Rabi frequency $\Omega_R = g_x h_x/\hbar$. Importantly, we note that the large effective g -factor in the x direction enables ultrafast single-qubit gate operations, achieving a gate time of 0.1 ns with a field amplitude of $h_x \sim 10$ mT.

DMRG for coupled DWs.—We now investigate the interactions between quantum DW textures using DMRG. To this end, we consider a quantum spin ladder [27] com-

posed of two identical spin chains weakly coupled at a single site in the middle of the chains ($N_c = 15$), as shown in Fig. 3(a). Each chain contains a total of N_x sites. We first focus on the coupling between two stationary DW qubits, where the DW centers are pinned to the middle of each chain by h_z [see Fig. 3(a)]. The spin ladder Hamiltonian is given by: $H_{\text{ladder}} = H_{\text{chain},1} + H_{\text{chain},2} + H_{\text{in}}$, where the interaction Hamiltonian is $H_{\text{in}} = -J_{\text{in}} \mathbf{S}_{N_c,1} \cdot \mathbf{S}_{N_c,2}$ and $H_{\text{chain},1(2)}$ represents the single chain Hamiltonian defined in Eq. (1). The two spin chains are weakly coupled ferromagnetically at site N_c , with J_{in} satisfying $0 < J_{\text{in}} \ll J$. We point out that the single-site inter-chain coupling is effectively equivalent to a uniform inter-chain coupling with reduced strength as shown in SM [25].

We calculate the energy levels of the first four eigenstates of the two coupled DWs, which form a well-isolated two-qubit subspace. The energy levels as functions of h_x are shown in Figs. 3(b-e). We observe that, in the absence of inter-chain coupling [Fig. 3(b)], the first excited state ($E_{1,2}$) is degenerate, corresponding to a mixed state of opposite DW chiralities in each spin chain. Importantly, when the inter-chain coupling J_{in} is introduced, the interaction between the two DW qubits lifts this degeneracy, opening a gap between the E_1 and E_2 states, as seen in Fig. 3(c-e). This interaction between DW qubits enables the implementation of two-qubit gates, which will be discussed in detail later. From the DMRG simulations, we extrapolate the effective Hamiltonian for the two coupled DW qubits:

$$H_2^{\text{eff}} = H_1^{\text{eff}} \otimes I_2 + I_1 \otimes H_2^{\text{eff}} - J_{\text{in}}^{\text{eff}} \sigma_x \otimes \sigma_x, \quad (4)$$

where $J_{\text{in}}^{\text{eff}}$ is the effective coupling strength of two DW qubits. The inter-chain coupling induces hybridization of chirality states between the two DW qubits, represented by the term ($\propto \sigma_x \otimes \sigma_x$) in the effective Hamiltonian. The effective coupling strength $J_{\text{in}}^{\text{eff}}$ scales approximately linearly with J_{in} in H_{in} . Notably, in the absence of the h_x field, the energy gap Δ_{21} is directly proportional to the inter-chain coupling, $\Delta_{21} = 2J_{\text{in}}^{\text{eff}}$, allowing the effective coupling strength to be easily extrapolated from DMRG simulations [25].

Effective coupling between moving DWs.—Two-qubit gates can be achieved by shuttling two DWs toward each other. To investigate this process, we consider a longer spin ladder with inter-chain coupling located at the center of the chains ($N_x = 61$, $N_c = 31$), while the length of each DW is fixed as $N = 30$. As schematically shown in Fig. 4(a), the positions of the pinning field h_z for each DW are shifted in a symmetric manner such that the center of the DWs translates in opposite directions and passes by the coupling site.

We then calculate the energy levels of the two-qubit subspace from DMRG simulation as a function of the displacement of the DWs from the center of the spin chains, denoted as ΔN , during their motion. This is shown in

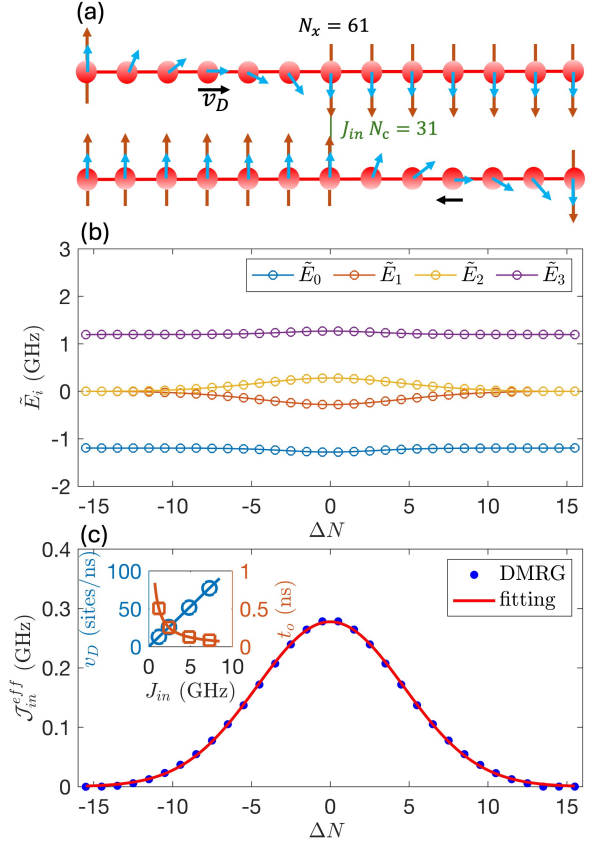


FIG. 4. (a) Schematic illustration of DMRG simulation for two moving DW qubits. (b) Energy levels of two-qubit computational space for two moving DW qubits with displacement of DW center ΔN . (c) Effective two-qubit coupling $J_{\text{in}}^{\text{eff}} = \Delta_{21}/2$ as function of displacement of DW center and Gaussian profile with fitting parameters $J_{\text{in}}^{\text{eff}} = 278$ MHz and $N_D = 6.58$. Single-site coupling strength is $J_{\text{in}} = 2.42$ GHz. The inset shows the required DW velocity v_D and operation time t_0 as function of single-site coupling strength. Parameters for each DW qubit are the same as in Fig. 1.

Fig. 4(b). We observe that, when the DW centers are far apart with $\Delta N \gg N$, the hybridization gap Δ_{21} vanishes. On the other hand, Δ_{21} reaches the maximum when the DW centers coincide with $\Delta N = 0$. As shown in Fig. 4(c), we find that the effective coupling strength between the two moving DWs, as a function of DW displacement ΔN , is well-fitted by a Gaussian profile:

$$J_{\text{in}}^{\text{eff}}(\Delta N) = J_{\text{in}}^{\text{eff}} \exp[-(\Delta N/N_D)^2], \quad (5)$$

where $J_{\text{in}}^{\text{eff}}$ represents the maximum coupling when the two DWs coincide, and N_D defines the characteristic range over which the mobile DWs interact. The fitted value of N_D is approximately 6.66 sites, which is comparable to the DW width. Therefore, through this quantum simulation, we demonstrate that the interaction between DWs remains significant when their separation is less than the DW width, beyond which the interaction

rapidly decays.

This position-dependent effective interaction can be further utilized to implement two-qubit gate operations. To this end, we consider two DWs moving toward the coupling site at a velocity $v_D = \Delta N/t$, where v_D represents the DW velocity in units of site/ns. In the interaction picture, the two-qubit interacting Hamiltonian reads $\tilde{H}_2 \approx -\mathcal{J}_{\text{in}}^{\text{eff}}(\Delta N)(\sigma_x \otimes \sigma_x + \sigma_y \otimes \sigma_y)$, when the qubit frequency is much faster than the coupling rate between DW qubits. Integrating over the Gaussian profile, the DW interaction yields a two-qubit gate operation

$$U_2 = \exp \left[\frac{i\sqrt{\pi}J_{\text{in}}^{\text{eff}}N_D}{\hbar v_D} (\sigma_x \otimes \sigma_x + \sigma_y \otimes \sigma_y) \right]. \quad (6)$$

For a DW with velocity $v_D = 4J_{\text{in}}^{\text{eff}}N_D/(\sqrt{\pi}\hbar)$, the unitary operation U_2 acts as an XY gate, which is equivalent to a controlled-NOT gate up to single-qubit rotations. Together with single qubit rotations, we then have a set of universal quantum gates. From the Gaussian fitting in Fig. 4(c), we extract the amplitude of the effective coupling as $J_{\text{in}}^{\text{eff}} = 278$ MHz and the interaction range as $N_D = 6.58$, corresponding to a DW velocity of $v_D = 25.9$ sites/ns and an ultrafast two-qubit gate operation time of approximately 0.25 ns. For a typical atomic spacing of approximately 5 Å, this corresponds to a DW velocity of ~ 12 m/s, which is feasible with recent advancements in spintronic techniques [3, 4]. Importantly, the interaction range between two DWs, characterized by N_D , is independent of the single-site coupling strength J_{in} . Consequently, the required DW velocity exhibits a linear dependence on J_{in} , while the operation time t_o is inversely proportional to J_{in} , as shown in Fig. 4(c). As the inter-chain coupling can be tuned, for instance, by adjusting the distance between spin chains, our system offers flexibility in controlling the operational time of the two-qubit gate.

Conclusion.—We have demonstrated the feasibility of utilizing DWs as qubits for universal quantum computation in a fully quantum framework. Through DMRG simulations, we established the existence of a well-defined low-energy subspace formed by DW chirality states, enabling robust quantum information encoding. The tunability of qubit splittings via magnetic fields, characterized by anisotropic effective g -factors, offers a practical way for implementing single-qubit gates. Moreover, we constructed an effective Hamiltonian for two interacting DW qubits, revealing the mechanism for generating entanglement and implementing two-qubit gates. Our work marks a pivotal step from semiclassical treatment to a fully quantum framework of nanoscale topological spin textures. By bridging this critical gap, we establish a solid foundation for utilizing topological spin textures in universal quantum computation.

This work was supported by the Georg H. Endress Foundation and by the Swiss National Science Foundation, NCCR SPIN (grant number 51NF40-180604).

T. H. is supported by JSPS KAKENHI Grant Number JP23K13064. The codes of DMRG simulations are written based on the ITensor Library [28].

-
- [1] J. Zang, V. Cros, and A. Hoffmann, *Topology in magnetism*, Vol. 192 (Springer, 2018).
 - [2] G. Nataf, M. Guennou, J. Gregg, D. Meier, J. Hlinka, E. Salje, and J. Kreisel, Domain-wall engineering and topological defects in ferroelectric and ferroelastic materials, *Nature Reviews Physics* **2**, 634 (2020).
 - [3] S.-H. Yang, K.-S. Ryu, and S. Parkin, Domain-wall velocities of up to 750 m s⁻¹ driven by exchange-coupling torque in synthetic antiferromagnets, *Nature nanotechnology* **10**, 221 (2015).
 - [4] K.-J. Kim, S. K. Kim, Y. Hirata, S.-H. Oh, T. Tono, D.-H. Kim, T. Okuno, W. S. Ham, S. Kim, G. Go, Y. Tserkovnyak, A. Tsukamoto, T. Moriyama, K.-J. Lee, and T. Ono, Fast domain wall motion in the vicinity of the angular momentum compensation temperature of ferromagnets, *Nature Mater* **16**, 1187 (2017).
 - [5] S. S. Parkin, M. Hayashi, and L. Thomas, Magnetic domain-wall racetrack memory, *science* **320**, 190 (2008).
 - [6] H.-B. Braun and D. Loss, Berry's phase and quantum dynamics of ferromagnetic solitons, *Phys. Rev. B* **53**, 3237 (1996).
 - [7] C. Psaroudaki and C. Panagopoulos, Skyrmion Qubits: A New Class of Quantum Logic Elements Based on Nanoscale Magnetization, *Phys. Rev. Lett.* **127**, 067201 (2021).
 - [8] J. Xia, X. Zhang, X. Liu, Y. Zhou, and M. Ezawa, Universal Quantum Computation Based on Nanoscale Skyrmion Helicity Qubits in Frustrated Magnets, *Phys. Rev. Lett.* **130**, 106701 (2023).
 - [9] S. Takei and M. Mohseni, Quantum control of topological defects in magnetic systems, *Phys. Rev. B* **97**, 064401 (2018).
 - [10] J. Zou, S. Bosco, B. Pal, S. S. P. Parkin, J. Klinovaja, and D. Loss, Quantum computing on magnetic racetracks with flying domain wall qubits, *Phys. Rev. Research* **5**, 033166 (2023).
 - [11] D. P. DiVincenzo, The physical implementation of quantum computation, *Fortschritte der Physik: Progress of Physics* **48**, 771 (2000).
 - [12] M. Yamamoto, S. Takada, C. Bäuerle, K. Watanabe, A. D. Wieck, and S. Tarucha, Electrical control of a solid-state flying qubit, *Nature Nanotech* **7**, 247 (2012).
 - [13] J. Zou, S. Bosco, J. Klinovaja, and D. Loss, Topological spin textures enabling quantum transmission, arXiv preprint arXiv:2409.14373 (2024).
 - [14] S. R. White, Density matrix formulation for quantum renormalization groups, *Phys. Rev. Lett.* **69**, 2863 (1992).
 - [15] U. Schollwöck, The density-matrix renormalization group, *Rev. Mod. Phys.* **77** (2005).
 - [16] M. Fishman, S. R. White, and E. M. Stoudenmire, The ITensor Software Library for Tensor Network Calculations, *SciPost Phys. Codebases*, 4 (2022).
 - [17] R. Schilling, Quantum theory of domain walls, *Phys. Rev. B* **15**, 2700 (1977).
 - [18] F. C. Alcaraz, S. R. Salinas, and W. F. Wreszinski, Anisotropic Ferromagnetic Quantum Domains, *Phys.*

- Rev. Lett.* **75**, 930 (1995).
- [19] F. C. Alcaraz, A. Saguia, and M. S. Sarandy, Entanglement and quantum phases in the anisotropic ferromagnetic Heisenberg chain in the presence of domain walls, *Phys. Rev. A* **70**, 032333 (2004).
- [20] H.-B. Braun and D. Loss, Chirality correlation of spin solitons: Bloch walls, spin- $\frac{1}{2}$ solitons and holes in a 2d antiferromagnetic background, *International Journal of Modern Physics B* **10**, 219 (1996), <https://doi.org/10.1142/S021797929600009X>.
- [21] J. Kyriakidis and D. Loss, Bloch oscillations of magnetic solitons in anisotropic spin- $\frac{1}{2}$ chains, *Phys. Rev. B* **58**, 5568 (1998).
- [22] Y. Tserkovnyak, J. Zou, S. K. Kim, and S. Takei, Quantum hydrodynamics of spin winding, *Phys. Rev. B* **102**, 224433 (2020).
- [23] J. Zou, S. Zhang, and Y. Tserkovnyak, Topological transport of deconfined hedgehogs in magnets, *Phys. Rev. Lett.* **125**, 267201 (2020).
- [24] Y. Tserkovnyak and J. Zou, Quantum hydrodynamics of vorticity, *Phys. Rev. Res.* **1**, 033071 (2019).
- [25] See Supplemental Material.
- [26] S. Bosco, S. Geyer, L. C. Camenzind, R. S. Eggli, A. Fuhrer, R. J. Warburton, D. M. Zumbühl, J. C. Egues, A. V. Kuhlmann, and D. Loss, Phase-Driving Hole Spin Qubits, *Phys. Rev. Lett.* **131**, 197001 (2023).
- [27] A. M. Läuchli and J. Schliemann, Entanglement spectra of coupled $S = 1/2$ spin chains in a ladder geometry, *Phys. Rev. B* **85**, 054403 (2012).
- [28] Itensor library, <https://github.com/ITensor> (2024).

Supplemental Material: “Density Matrix Renormalization Group Study of Domain Wall Qubits”

Guanxiong Qu¹, Ji Zou², Daniel Loss^{1,2,3}, Tomoki Hirose⁴

1. RIKEN, Center for Emergent Matter Science (CEMS), Wako-shi, Saitama 351-0198, Japan

2. Department of Physics, University of Basel, Klingelbergstr. 82, 4056 Basel, Switzerland

3. RIKEN, Center for Quantum Computing (RQC), Wako-shi, Saitama 351-0198, Japan

4. College of Science and Engineering, Aoyama Gakuin University, Japan

December 17, 2024

DMRG SIMULATIONS ON A SINGLE DW QUBIT

Effect of in-plane anisotropy K_y

In Figure 5, we illustrate the tuning of in-plane anisotropy (K_y) for both odd ($N = 31$) and even ($N = 30$) single spin chains in the absence of an external magnetic field ($h_x = h_y = 0$). For XXZ spin chains ($K_y = 0$), the ground state of an N -even spin chain is non-degenerate, whereas the ground state of an odd spin chain is doubly degenerate. This distinction arises because the boundary interaction h_z lifts the Kramers degeneracy in N -even chains but not in N -odd chains [17]. However, with the introduction of K_y , the ground state E_0 and the first excited state E_1 of the N -even spin chain also become degenerate, effectively reducing the finite-size parity effect for sufficiently large in-plane anisotropy ($K_y > 0.04$ meV), as shown in Figure 5 (c). Furthermore, we observe that the in-plane anisotropy K_y also increases the energy gap Δ_{21} between the first degenerate subspace (computational qubit space) and the second degenerate subspace.

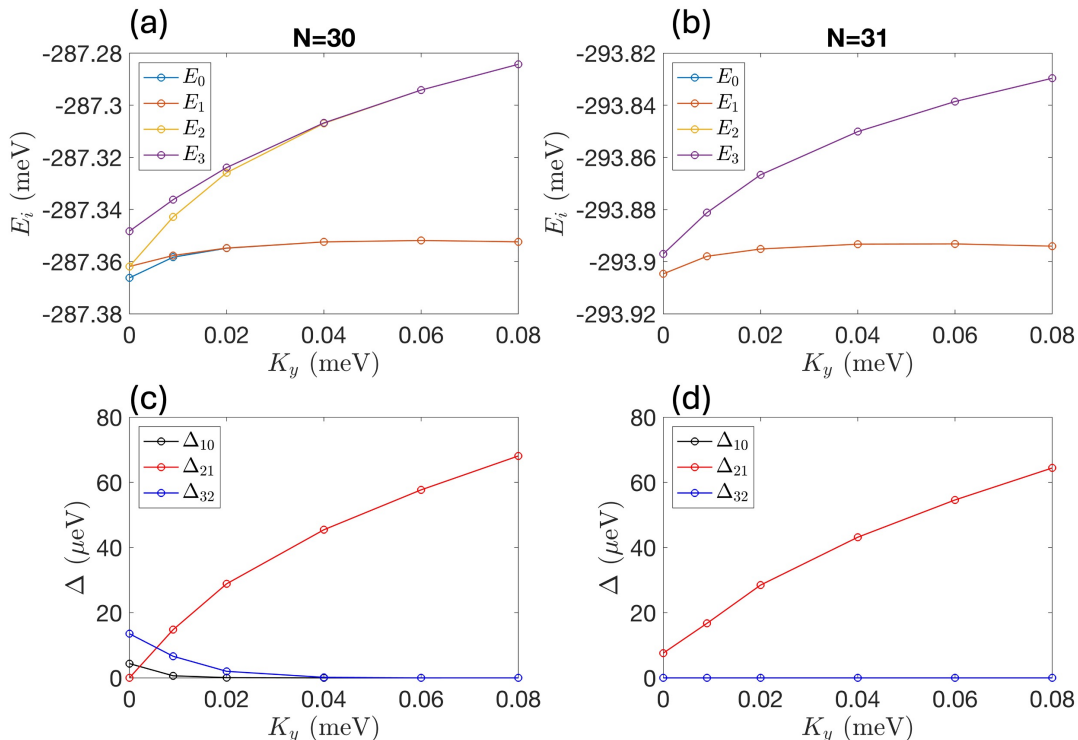


FIG. 5. Energy spectra of (a,b) the four lowest-lying states E_i and (c,d) the energy gaps $\Delta_{ij} \equiv E_i - E_j$ as tuned by in-plane anisotropy K_y for even $N = 30$ (left panel) and odd $N = 31$ (right panel) spin chains. The parameters used in the DMRG simulations are $J = 25.85$ meV, $K_z = 0.26$ meV, and $\mu_B h_z = -100$ meV. The criterion of energy convergence is at least 10^{-10} meV.

Effect of external magnetic fields h_x, h_y

In Figure 6, we demonstrate the effect of external magnetic fields on the qubit splitting Δ_{10} and the gap between the qubit space and higher energy levels Δ_{21} of a single DW qubit. The gap Δ_{21} decreases linearly with increasing h_x until Δ_{21} closes, while the qubit splitting Δ_{10} increases linearly with h_x , independent of the magnitude of in-plane anisotropy K_y [see Figure 6(a,c)]. In contrast, the h_y field causes an exponential increase in Δ_{10} beyond certain thresholds [10], while Δ_{21} is only minimally affected by the h_y field. These thresholds for qubit splitting opening with the h_y field grow as the in-plane anisotropy K_y increases.

To construct the DW qubit, a bias h_y field is preferred for opening the qubit splitting Δ_{10} , as it exponentially increases Δ_{10} while keeping Δ_{21} nearly unchanged. A small h_x field can be employed as a tuning field for the DW qubit due to its linear relationship with the qubit splitting $\Delta_{10} \propto h_x$. In the main text, we choose $K_y = 0.1$ meV and $h_y = 0.9$ T, where the qubit splitting is $\Delta_{10} \sim 4 \mu\text{eV}$ and the gap between the qubit space and higher levels is $\Delta_{21} \sim 40 \mu\text{eV}$. Thus, the qubit subspace is separated by a gap from the higher energy levels.

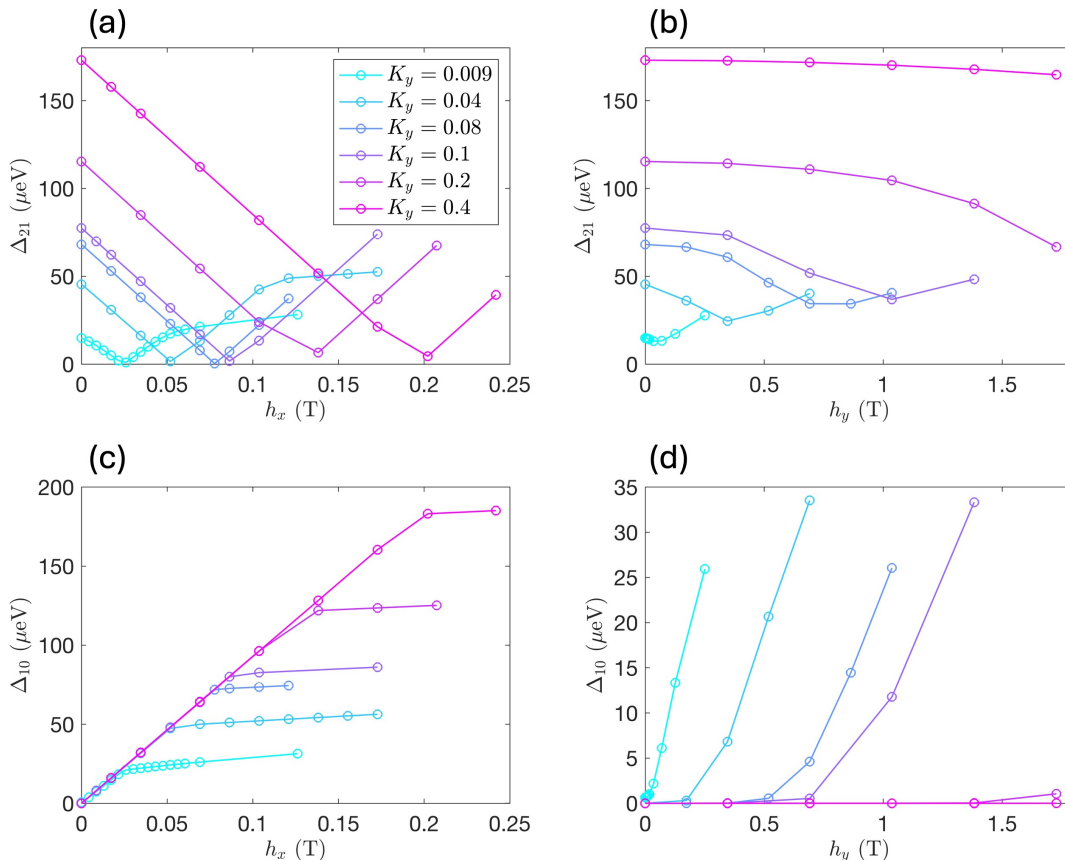


FIG. 6. (a,b) qubit splitting Δ_{10} and (c,d) the gap between the qubit space and higher energy levels Δ_{21} , tuned by external fields h_x and h_y under various in-plane anisotropies K_y . The parameters used in the DMRG simulations are $N = 30$, $J = 25.85$ meV, $K_z = 0.26$ meV, and $\mu_B h_z = -100$ meV. The criterion of energy convergence is at least 10^{-10} meV.

Comparison between N -even and N -odd spin chains

In Figure 7, we compare spin-1/2 chains with an even and an odd number N of sites. For a sufficiently large $K_y = 0.26$ meV, no significant difference is observed between the even and odd number chains, and both require a substantial bias field ($h_y \sim 0.9$ T) to open the qubit gap.

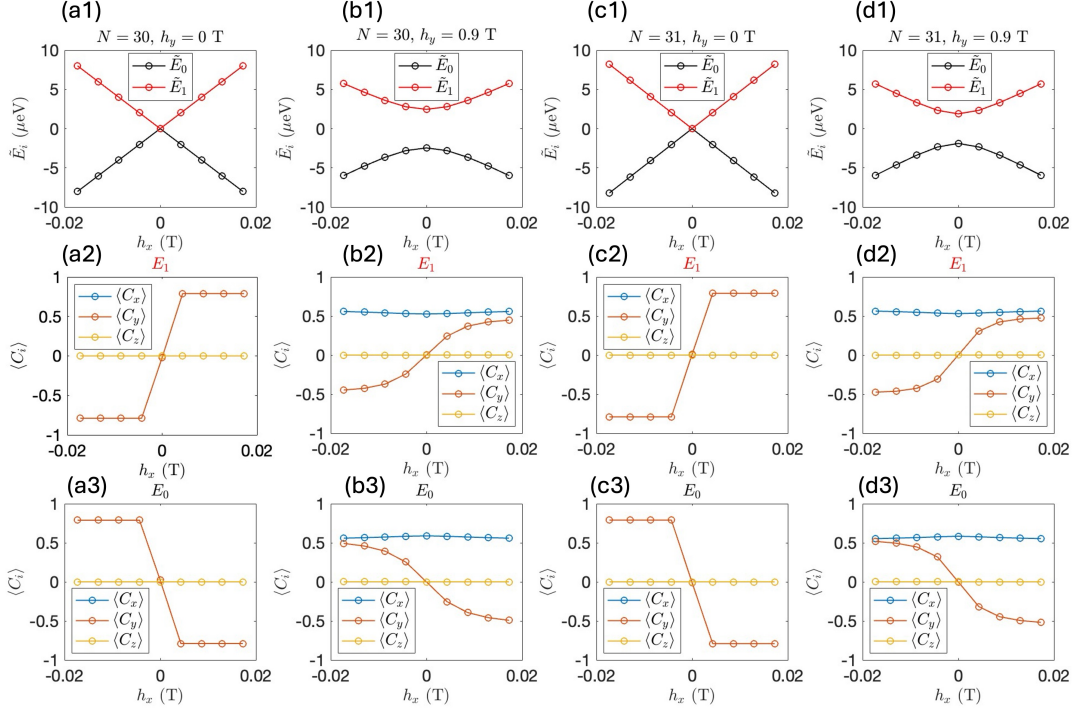


FIG. 7. DMRG simulation data of (1) DW qubits energy spectra and (2,3) DW chiralities of each qubit states with tuning of external magnetic fields h_x for (a,b) even number spin chains and (c,d) odd number spin chain. The parameters used in the DMRG simulations are $N = 30, 31$, $J = 25.85$ meV, $K_z = 0.26$ meV, $K_y = 0.1$ meV, and $\mu_B h_z = -100$ meV. The criterion of energy convergence is at least 10^{-10} meV.

DMRG SIMULATIONS ON COUPLED DW QUBITS

Uniform inter-chain coupling

We consider two DW spin chains uniformly coupled at each site [see Figure 8 (a)]. The inter-chain coupling Hamiltonian reads

$$H_{inter} = -J_{in} \sum_{i=1}^N \mathbf{S}_{i,1} \cdot \mathbf{S}_{i,2}, \quad (7)$$

where $J_{in} > 0$ denotes ferromagnetic coupling constant uniformly across the spin chains.

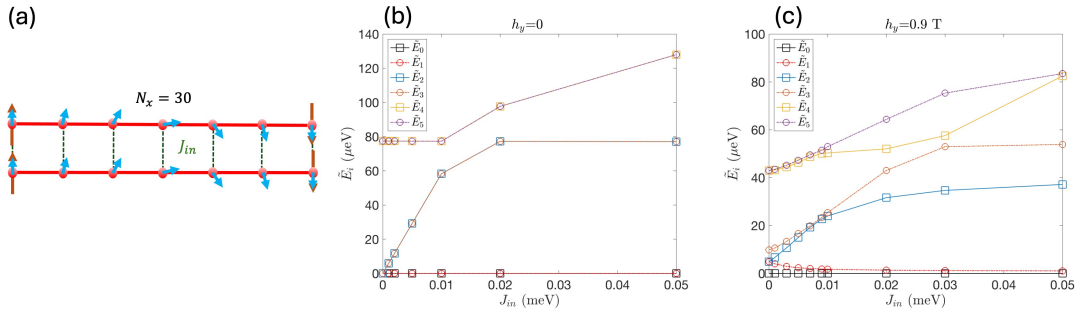


FIG. 8. (a) Schematic plot of two uniformly coupled DW qubits. Energy spectra of spin ladders with inter-chain coupling J_{in} at (a) $h_y = 0$ T and (b) $h_y = 0.9$ T. The parameters used in the DMRG simulations are $N = 30$, $J = 25.85$ meV, $K_z = 0.26$ meV, $K_y = 0.1$ meV, and $\mu_B h_z = -100$ meV. The criterion of energy convergence is at least 10^{-10} meV.

Figure 8 (b,c) presents the energy spectra of two coupled spin chains against the inter-chain coupling strength J_{in} . Note that the DW qubit splitting closes on a single spin chain without applying the h_y field. On coupled spin

chains, the DW qubit splitting on each chain remains closed without h_y fields, resulting in four degenerate states at $J_{in} = 0$. As the inter-chain coupling is turned on, the four degenerate states split into doubly degenerate “bonding” and “anti-bonding” states between the two spin chains, as shown in Fig. 8(b). Notably, the gap between the “bonding” and “anti-bonding” states saturates at a very small inter-chain coupling strength $J_{in} \sim 0.02$ meV, compared to the intra-chain coupling $J = 25.85$ meV.

When the h_y field is applied, the DW qubit splitting emerges in each spin chain. The two levels of the DW qubit are labeled as $|0\rangle = (|\odot\rangle + |\ominus\rangle)/\sqrt{2}$ and $|1\rangle = (|\odot\rangle - |\ominus\rangle)/\sqrt{2}$. In the absence of inter-chain coupling ($J_{in} = 0$), two identical spin chains remain decoupled, where the coupled DW qubit subspace exhibits three energy levels with corresponding eigenstates: $|00\rangle$, $|01\rangle/|10\rangle$, and $|11\rangle$, where $|01\rangle$ and $|10\rangle$ are the doubly degenerate states. The introduction of inter-chain coupling lifts the degeneracy of the $|01\rangle$ and $|10\rangle$ states, resulting in two “bonding” and “anti-bonding” pairs of states in the coupled DW qubit subspace, as illustrated in Fig. 8(c). The gap between the “bonding” and “anti-bonding” pairs nearly saturates at $J_{in} \sim 0.02$ meV, similar to the case without the h_y field. In the following, we focus on the regime where the two spin chains are weakly coupled ($J_{in} < 5$ μeV), and the “bonding” and “anti-bonding” pairs are moderately gapped.

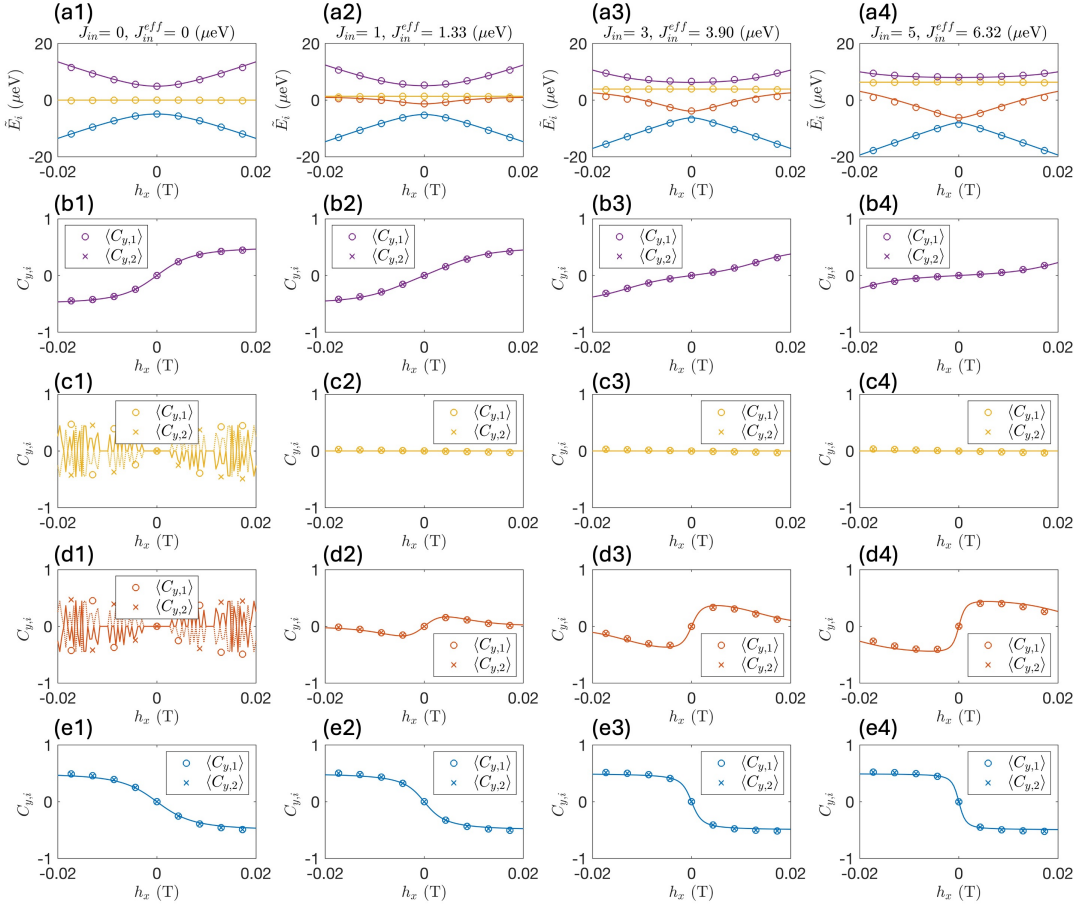


FIG. 9. DMRG simulation data (circles and crosses) and effective model data (lines) of (a) energy spectra and (b-e) domain wall chirality $C_{y,i}$ of each spin chain ($i = 1, 2$) with various inter-chain coupling strength $J_{in} = 0, 1, 3, 5$ μeV and corresponding effective coupling strength $J_{in}^{eff} = 0, 1.33, 3.90, 6.32$ μeV . The parameters used in the DMRG simulations are $N = 30$, $J = 25.85$ meV, $K_z = 0.26$ meV, $K_y = 0.1$ meV, $h_y = 0.9$ T, and $\mu_B h_z = -100$ meV. The criterion of energy convergence is at least 10^{-10} meV.

Figure 9 (a) shows the energy spectra of DW qubits under varying h_x fields for different inter-chain coupling strengths, $J_{in} = 0, 1, 3, 5$ μeV . As the inter-chain coupling strength J_{in} increases, the energy gap between the $|01\rangle$ and $|10\rangle$ states widens, indicating an interaction between the two DW qubits. We also present the DW chiralities $C_{y,i}$ of each spin chain ($i = 1, 2$) for each energy level in the DW qubit subspace, as shown in Figure 9 (b-e). Remarkably, the chiralities $C_{y,i}$ of the two spin chains always coincide, suggesting that the spin chains exhibit coherent interaction under ferromagnetic inter-chain coupling. For decoupled spin chains ($J_{in} = 0$), we find that the two non-degenerate

states E_0 and E_3 have opposite DW chiralities, while the expectation value of DW chirality for the doubly degenerate states is zero [see Fig. 9 (c1,d1)]. As J_{in} increases, the DW chiralities $C_{y,i}$ for the E_3 -states decrease, while $C_{y,i}$ for the E_1 -states increase.

Effective Hamiltonian of coupled domain wall qubit

We recall the effective Hamiltonian of coupled DW qubits shown in the main text [Eq. (9)]:

$$H_2^{\text{eff}} = H_1^{\text{eff}} \otimes I_2 + I_2 \otimes H_1^{\text{eff}} - J_{in}^{\text{eff}} \sigma_x \otimes \sigma_x$$

$$= \begin{pmatrix} \Delta_{10} + 2g_y \Delta h_y & -g_x h_x & -g_x h_x & -J_{in}^{\text{eff}} \\ -g_x h_x & 0 & -J_{in}^{\text{eff}} & -g_x h_x \\ -g_x h_x & -J_{in}^{\text{eff}} & 0 & -g_x h_x \\ -J_{in}^{\text{eff}} & -g_x h_x & -g_x h_x & -\Delta_{10} - 2g_y \Delta h_y \end{pmatrix}. \quad (8)$$

Without driving fields ($h_x = 0$, $\Delta h_y = 0$), the eigenenergies of the coupled DW qubits are trivial: $\pm J_{in}^{\text{eff}}$, $\pm \sqrt{\Delta_{10}^2/4 + J_{in}^{\text{eff}2}}$. For weak coupling ($J_{in}^{\text{eff}} < \Delta_{10}/2$), the energy gap between the $|01\rangle$ and $|10\rangle$ states is proportional to the effective inter-chain coupling, $\Delta_{21} \equiv E_2 - E_1 = 2J_{in}^{\text{eff}}$. Thus, the effective inter-chain coupling strength J_{in}^{eff} in Eq. (8) can be easily extrapolated from the gap size Δ_{21} in DMRG simulations. The DW chirality operator for each spin chain in the effective Hamiltonian is defined as $\hat{C}_{y,1} = \frac{1}{2}\sigma_x \otimes I_2$, $\hat{C}_{y,2} = \frac{1}{2}I_2 \otimes \sigma_x$. Figure 9 shows the energy spectra and corresponding DW chiralities of each energy level with J_{in}^{eff} extrapolated from DMRG simulations. The data from the effective Hamiltonian calculation are consistent with DMRG simulations.

Single-site inter-chain coupling

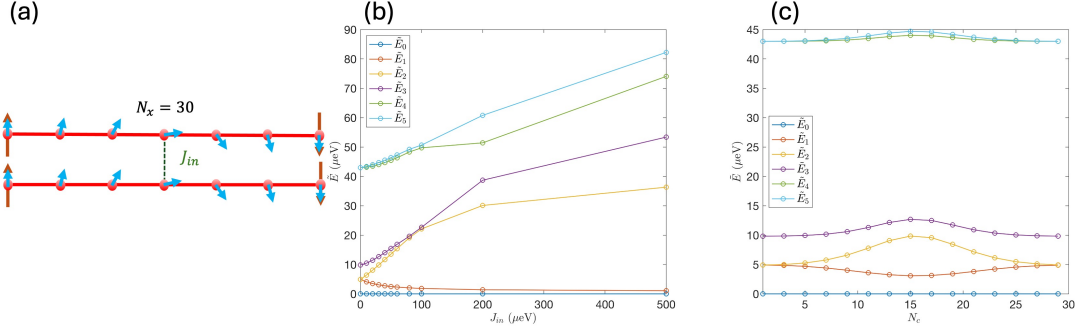


FIG. 10. (a) Schematic plot of single-site coupled DW qubits. Energy spectra of coupled DW qubits with (b) fixed coupling site ($N_c = 15$) and (c) fixed coupling strength $J_{in} = 30 \mu\text{eV}$. The parameters used in the DMRG simulations are $N = 30$, $J = 25.85 \text{ meV}$, $K_z = 0.26 \text{ meV}$, $K_y = 0.1 \text{ meV}$, and $\mu_B h_z = -100 \text{ meV}$. The criterion of energy convergence is at least 10^{-10} meV .

For single-site coupled spin chains [see Fig. 10 (a)], the inter-chain coupling Hamiltonian is

$$H_{inter} = -J_{in} \mathbf{S}_{N_c,1} \cdot \mathbf{S}_{N_c,2}, \quad (9)$$

where N_c is the site at which the two spin chains are exchange coupled.

Figure 10(b) shows energy spectra of the single-site coupled spin chains against the inter-chain coupling strength J_{in} . The energy spectra show the same profile as uniformly coupled spin chains, Fig. 8(c), while the magnitude of coupling strength required to open the same gap Δ_{12} is one order of magnitude larger. The energy spectra at different coupling sites is shown in Fig. 10(c). The interaction between two DW qubits reaches its maximum at the center of DWs and is nearly zero at the boundaries. We also confirm that the two-qubit subspace with the single-site coupling and uniform coupling is equivalent with small J_{in} , see Fig. 11.

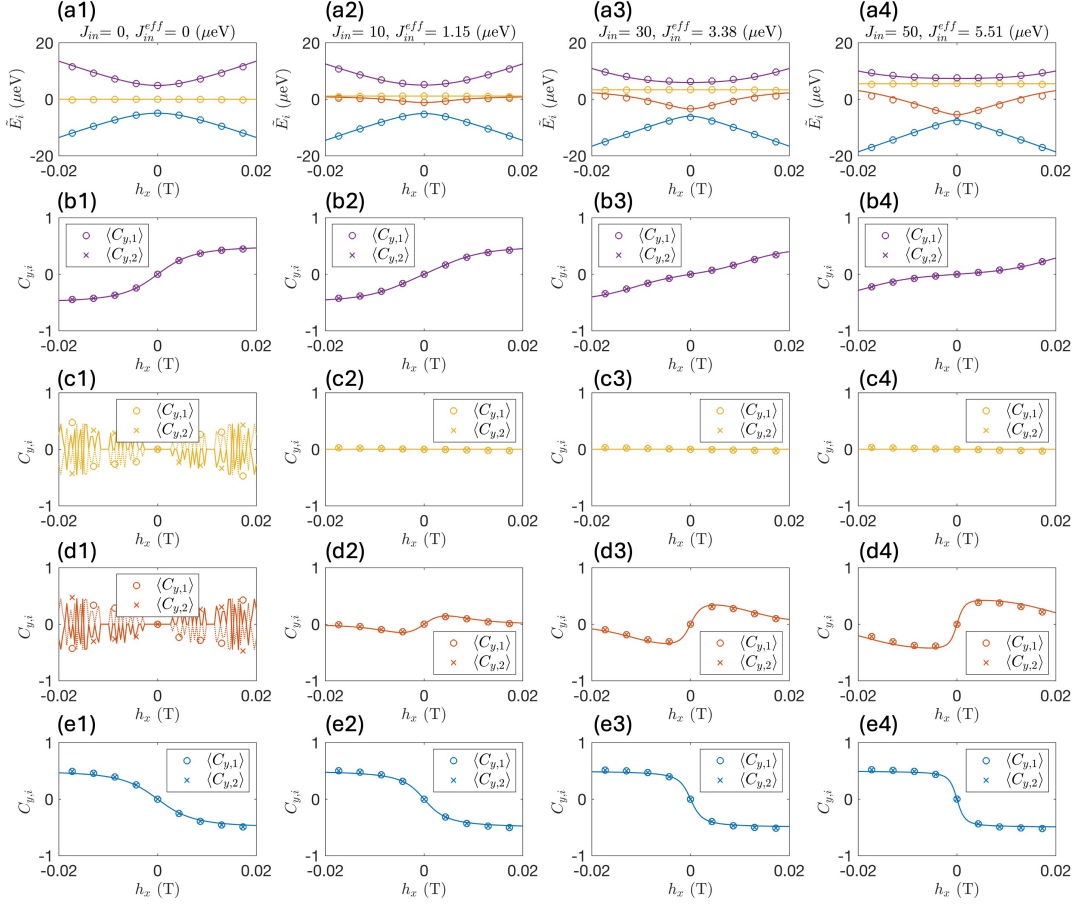


FIG. 11. DMRG simulation data (circles and crosses) and effective model data (lines) of (a) energy spectra and (b-e) domain wall chirality $C_{y,i}$ of each spin chain ($i = 1, 2$) with various single-site inter-chain coupling strength $J_{in} = 0, 10, 30, 50 \mu\text{eV}$ and corresponding effective coupling strength $J_{in}^{eff} = 0, 1.15, 3.38, 5.51 \mu\text{eV}$. The parameters used in the DMRG simulations are $N = 30$, $J = 25.85 \text{ meV}$, $K_z = 0.26 \text{ meV}$, $K_y = 0.1 \text{ meV}$, $h_y = 0.9 \text{ T}$, and $\mu_B h_z = -100 \text{ meV}$. The criterion of energy convergence is at least 10^{-10} meV .

Two mobile domain walls

Figure 12(a) displays the energy spectra of two mobile DWs as a function of the displacement between their centers, ΔN . As the single-site coupling strength J_{in} increases, the energy gap Δ_{21} widens, indicating stronger coupling as the two DWs move closer to each other. The effective coupling strengths J_{in}^{eff} , extrapolated from DMRG simulations, are fitted with Gaussian profiles of ΔN , see Fig. 12(b). The amplitude of these Gaussian profiles scales with J_{in} , while the coupling regime between the two mobile DWs, N_D , remains constant.

QUBIT GATE OPERATIONS

single qubit gate operation

For a single DW qubit, the Rabi-driving Hamiltonian reads:

$$H_1^{\text{Rabi}} = \frac{\hbar\omega_q}{2}\sigma_z - g_x h_x \cos(\omega_x t)\sigma_x, \quad (10)$$

where $\hbar\omega_q = \Delta_{10}$. In the rotating frame, ignoring higher-order harmonics, the Hamiltonian reads:

$$\tilde{H}_{\text{RWA}} = \frac{\hbar\Delta\omega}{2}\sigma_z - \frac{g_x h_x}{2}\sigma_x, \quad (11)$$

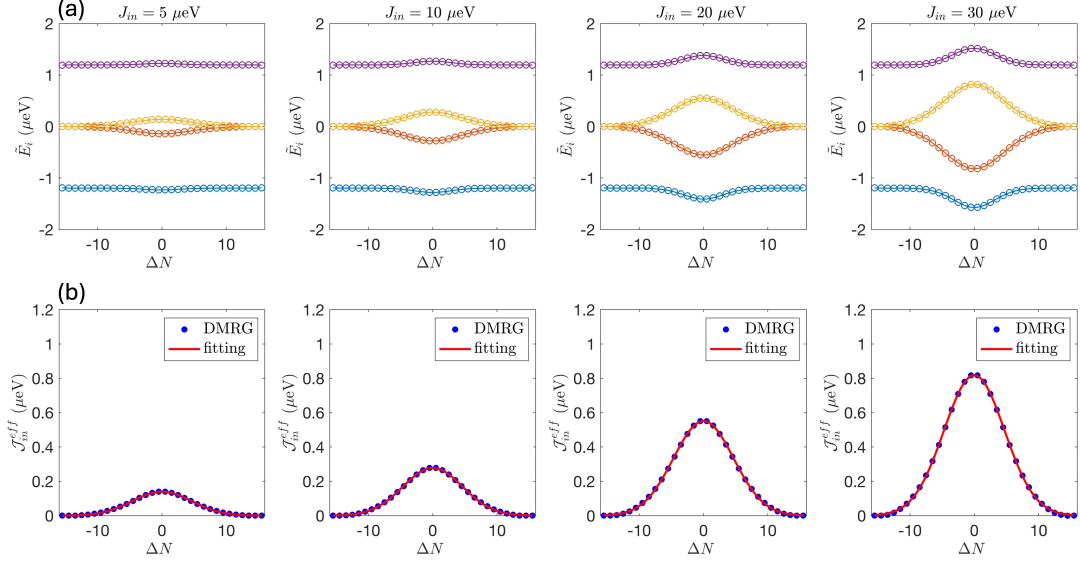


FIG. 12. DMRG simulation data of (a) energy spectra and (b) effective coupling strength as functions of the displacement of domain wall centers, ΔN , for various single-site coupling strengths $J_{in} = 5, 10, 20, 30 \mu\text{eV}$. The parameters used in the DMRG simulations are $N_x = 61$, $N_c = 31$, $N = 30$, $J = 25.85 \text{ meV}$, $K_z = 0.26 \text{ meV}$, $K_y = 0.1 \text{ meV}$, $h_y = 0.9 \text{ T}$, and $\mu_B h_z = -100 \text{ meV}$. The criterion of energy convergence is at least 10^{-9} meV .

where $\Delta\omega = \omega_q - \omega_x$. This yields the time-evolution operator:

$$U(t) = \exp \left\{ -i \left(\frac{\Delta\omega}{2} \sigma_z - \frac{g_x h_x}{2\hbar} \sigma_x \right) t \right\}. \quad (12)$$

which rotates the qubit state around the vector $\left(-\frac{g_x h_x}{2\hbar}, 0, \frac{\Delta\omega}{2} \right)$.

Coupled Qubit Gate Operation

When DW qubits pass by each other with coupling at their centers, the effective Hamiltonian is:

$$H_2^{\text{eff}} = \frac{\hbar\omega_q}{2} (\sigma_z \otimes I_2 + I_2 \otimes \sigma_z) - J_{in}^{\text{eff}}(\Delta N) \sigma_x \otimes \sigma_x, \quad (13)$$

The interaction Hamiltonian is:

$$\begin{aligned} \tilde{H}_{2,I}^{\text{eff}} &= -J_{in}^{\text{eff}}(\Delta N) \exp \left[i \frac{\omega_q t}{2} (\sigma_z \otimes I_2 + I_2 \otimes \sigma_z) \right] \sigma_x \otimes \sigma_x \exp \left[-i \frac{\omega_q t}{2} (\sigma_z \otimes I_2 + I_2 \otimes \sigma_z) \right] \\ &= -J_{in}^{\text{eff}}(\Delta N) \begin{pmatrix} 0 & 0 & 0 & e^{2i\omega_q t} \\ 0 & 0 & 1 & 0 \\ 0 & 1 & 0 & 0 \\ e^{-2i\omega_q t} & 0 & 0 & 0 \end{pmatrix} \\ &\approx -J_{in}^{\text{eff}}(\Delta N) (\sigma_x \otimes \sigma_x + \sigma_y \otimes \sigma_y), \end{aligned} \quad (14)$$

where we ignore the fast oscillating term ($2\omega_q$) in the last equation. The unitary gate operation for two DW qubits passing by each other is:

$$\begin{aligned} U_2 &= \exp \left\{ \frac{i}{\hbar} \int_{-\infty}^{\infty} dt J_{in}^{\text{eff}}(\Delta N) (\sigma_x \otimes \sigma_x + \sigma_y \otimes \sigma_y) \right\} \\ &= \exp \left\{ \frac{i J_{in}^{\text{eff}}}{\hbar v_D} \int_{-\infty}^{\infty} d(\Delta N) \exp [-(\Delta N / N_D)^2] (\sigma_x \otimes \sigma_x + \sigma_y \otimes \sigma_y) \right\} \\ &= \exp \left\{ \frac{i \sqrt{\pi} J_{in}^{\text{eff}} N_D}{\hbar v_D} (\sigma_x \otimes \sigma_x + \sigma_y \otimes \sigma_y) \right\}, \end{aligned} \quad (15)$$

where $v_D = \Delta N/t$ is the velocity of DW qubits (units in site/s).
